

Article

# Development of Ultrasonic Techniques for Measurement of Spatially Non-Uniform Elastic Properties of Thin Plates by Means of a Guided Sub-Sonic $A_0$ Mode

Rymantas Jonas Kazys \*, Liudas Mazeika and Justina Sestoke

Prof. K. Barsauskas Ultrasound Research Institute, Kaunas University of Technology, 51423 Kaunas, Lithuania; liudas.mazeika@ktu.lt (L.M.); justina.sestoke@ktu.lt (J.S.)

\* Correspondence: rymantas.kazys@ktu.lt; Tel.: +370-(37)-300-543

Received: 5 April 2020; Accepted: 7 May 2020; Published: 9 May 2020



**Abstract:** Air-coupled ultrasonic guided  $A_0$  mode is already used for material characterization. By measuring the phase velocity of the  $A_0$  mode the elastic properties, such as the Young's modulus, can be determined. The objective of this work was the development of measurement methods and corresponding signal processing procedures enabling the acquisition of spatial distributions of non-uniform elastic properties of thin films and plates. Those methods are based on the excitation of a slow sub-sonic  $A_0$  Lamb wave mode in a plate, the measurement of normal displacements at different distances from the source, the formation of the B-scan, and processing the collected signals. Two different signal processing methods were proposed and investigated. In the first method the all zero-crossing instants of the ultrasonic signals at different distances are found and from them spatial distributions of the  $A_0$  mode velocity are determined. According to the second method 2D spatial-temporal spectrum of the B-scan is calculated and propagating  $A_0$  modes with different velocities are identified. Efficiency of the proposed methods was evaluated theoretically and experimentally using thin mineral MICA paper samples, which is used in the electrical and aerospace industries as an insulating material. The zones with different  $A_0$  mode phase velocities ( $95 \pm \Delta 3$  m/s and  $(106 \pm \Delta 6$  m/s) at the frequency 47 kHz were identified.

**Keywords:** air-coupled ultrasonics; ultrasonic guided waves; Lamb waves; sub-sonic  $A_0$  mode; mineral MICA paper; non-destructive testing and evaluation

## 1. Introduction

Contemporary technologies are broadly employing composite plate materials developed by using various innovative materials (nanostructures, mica structures, etc.) [1]. Ultrasonic methods enable research of key properties of materials which cannot be assessed by merely using the traditional methods. The guided ultrasonic waves are extensively used for non-destructive testing and evaluation (NDT) of sheet type materials [2,3]. They are commonly excited when the vibrations of an acoustic transducer are transferred to the investigated item by a direct contact via a narrow gap of liquid. However, liquids are impossible to use in a wide range of cases as the item under investigation may be contaminated, damaged, or otherwise negatively affected. This is relevant to the research of paper, cardboard, membranes and composite structures which are used across a wide variety of fields including aerospace industry [4–9].

In this case the guided waves in sheet type objects are excited and picked-up via air gap using contactless air-coupled ultrasonic transducers. Usually for this purpose the lowest anti-symmetrical  $A_0$  mode is exploited [10–12]. This mode is dispersive, e.g., its phase velocity is frequency dependant and

is reducing with a reducing frequency [12–14]. In order to achieve efficient excitation and reception of such mode the air-coupled ultrasonic transducers are deflected according to the Snell's law. This mode is commonly applied for detecting of defects in composite materials as the leakage is extremely prominent at the defective site [14–18]. Attenuation of acoustic waves in air and in the investigated structure increases with the growth of the frequency; thus, in real life the frequency of ultrasonic waves is selected to be as low as possible. Usually, it does not exceed 1 MHz. The losses of ultrasonic non-destructive investigations may be reduced by generating the guided waves while using the lower frequencies (<100 kHz) [19,20]. With decrease of a frequency the sub-sonic or slow anti-symmetric Lamb  $A_0$  mode may be excited in which the phase velocity becomes lower than the velocity of sound in air. In this case, the slow guided waves propagating in the structure under investigation do not excite the leaky waves and may travel longer distances without losses [21,22]. However, application of conventional methods for excitation of the slow guided waves based on exploitation of air-coupled transducers deflected according to the Snell's law is not efficient. Due to those reasons at low frequencies for excitation of the guided waves via air gap it is sensible to employ ultrasonic low frequency arrays [23–25].

Propagation of the slow  $A_0$  mode within thin films is accompanied by evanescent waves in surrounding air whose amplitude decreases with the increase of the distance from the investigated films. This phenomenon can be employed for a non-contact reception of the  $A_0$  mode applying specially designed air-coupled ultrasonic arrays.

At the moment there are not many publications in which excitation and reception of a slow  $A_0$  mode is discussed. Various techniques used for such purposes were proposed and investigated by us [26,27]. For this purpose ultrasonic air-coupled arrays with high efficiency piezoelectric elements made of PMN-32%PT crystals were developed [26].

The elastic properties and/or thickness of thin plates and films can be estimated from the measured velocity of ultrasonic guided waves propagating in them. However, in the most of the published research the information about an internal structure of the object under investigation is obtained from ultrasonic signals which propagate some distance from the ultrasonic transmitter to the ultrasonic receiver. This means that in such cases only average values of the ultrasound velocity and, consequently, the elastic properties of the object can be determined and any information about spatial variations of those properties is lost. Of course, the spatial resolution may be improved by shortening the propagation path of the ultrasonic wave, for example, reducing the distance between the ultrasonic transmitter and receiver, but it unavoidably increases the measurement errors.

The objective of this work was development of measurement methods and corresponding signal processing procedures enabling to obtain spatial distributions of non-uniform elastic properties of a thin films and plates. Those methods are based on excitation of a slow sub-sonic  $A_0$  mode in a plate, measurement of normal displacements of the plate, formation of the B-scan and processing the collected signals. For a signal processing two different methods were proposed and investigated.

In the first method the all zero-crossing instants of the recorded ultrasonic signals at different distances are found and from them the delay time B-scan is formed. This B-scan is used to obtain spatial distributions of the  $A_0$  mode velocity in different parts of the plate or film under investigation.

The second method is based on calculation of the two-dimensional spatial-temporal spectrum of the primary B-scan of normal displacements. From this spectrum is possible to identify  $A_0$  modes propagating with different velocities. Strictly speaking this method does not provide a spatial distribution of ultrasound velocity in plates, but enables to measure velocities of different guided waves modes, for example  $A_0$  Lamb wave modes, which are caused by spatially non-uniform areas of the plate with different elastic properties and/or thickness. As it will be shown in this paper, some information about spatial distributions can be obtained by selecting a window in the spatial domain in which the 2D Fourier transform is performed.

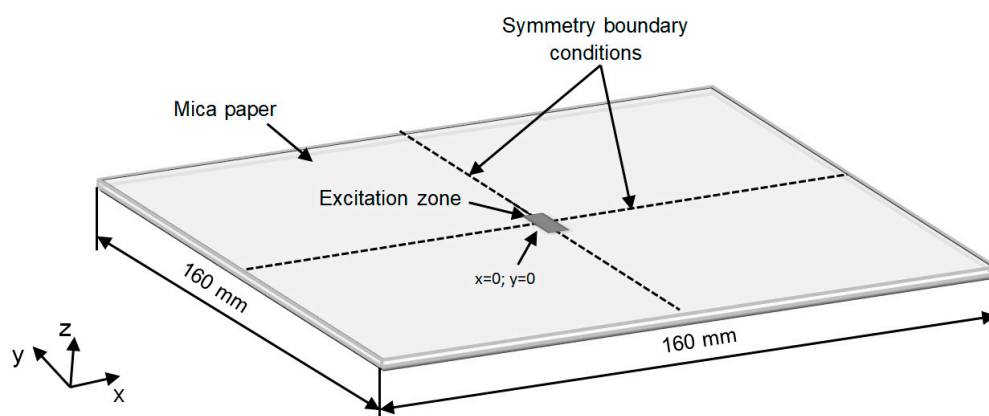
Efficiency of the proposed methods was investigated on mica paper samples. Mica is a naturally occurring mineral, consisting of aluminium, potassium, magnesium, iron, water, and possessing a thin

plate-like structure. The tensile strength of the mica is very low; therefore, it is reinforced according to the product with some backing, like glass cloth or polyethylene film. Mica is widely used in the electrical industry as an insulating material because it possesses a high dielectric strength. In the aerospace industry mica, due to its resistance to high compression at very high temperatures, is used for insulation of aircraft thrust reversal systems, where thermal protection is critical.

According to manufacturers the most important parameters of the mica paper are density, tensile strength, porosity, and uniformity of elastic properties. On-line measurement of those parameters, especially of the elastic properties and thickness during a manufacturing process, have not been solved up to now. The paper consists of five sections. A numerical modelling of propagation of the slow  $A_0$  mode in a thin mica paper is discussed in Section 2, the B-scan zero-crossing reconstruction method enabling spatial reconstruction of non-uniform elastic properties is described in Section 3, the 2D spatial-temporal spectrum method in Section 4, and the theoretical results are verified by measurements performed by a laser interferometer in Section 5.

## 2. Numerical Investigation

Propagation of the guided subsonic  $A_0$  mode in the mica paper sample was simulated by the Abaqus/CAE 2016.HF2 software package (Dassault Systemes, Johnston, Rhode Island, United States). Dimensions of the mica sample were  $160 \times 160$  mm. For reduction of the computational time, only a quarter of the paper with symmetry boundary conditions was modelled. The modelled structure is presented in Figure 1.



**Figure 1.** A model of the mica sample used for the simulation.

During the simulation it was assumed that there are zones with different elastic properties and thickness. The real MICA paper samples contain mica ore muscovite in optically lighter zones and phlogopite in darker zones, the elastic properties and thickness of which are different. In the darker zone thickness of the sample is  $d = 35 \mu\text{m}$ , the Young's modulus  $E_D = 16 \text{ GPa}$ , the Poisson's coefficient  $\nu = 0.25$ , the density  $\rho = 771 \text{ kg/m}^3$ . Correspondingly, in the lighter zone  $d = 30 \mu\text{m}$ ,  $E_L = 13 \text{ GPa}$ ,  $\nu = 0.25$ ,  $\rho = 771 \text{ kg/m}^3$ .

The simulation step in the time domain was  $dt = 1 \mu\text{s}$ . The excitation was applied at a rectangular zone  $5 \times 1 \text{ mm}^2$ , the centre of which was at  $x = 0$ ,  $y = 0$ . The excitation was introduced as the uniformly distributed  $1 \text{ N}$   $44 \text{ kHz}$  force impulse in the transmitter area. The frequency of  $44 \text{ kHz}$  was selected because at such a frequency only the slow  $A_0$  mode may propagate. The waveform and the spectrum of the excitation force are shown in Figure 2a,b.

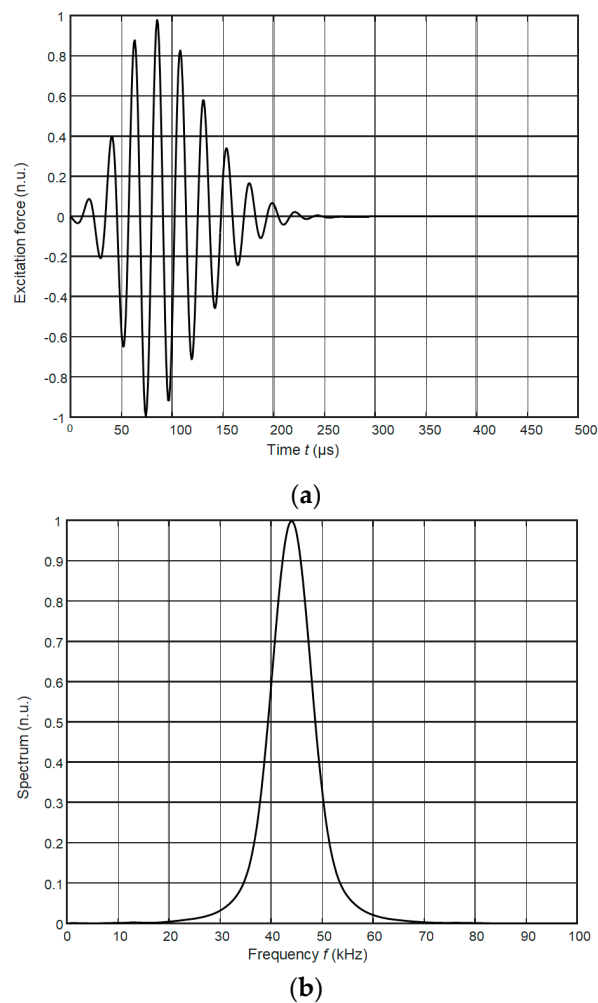


**Figure 2.** The waveform (a) and the spectrum of the excitation force (b); n.u. represents normalized units.

The model of the mica paper was meshed using shell elements. The shell thicknesses are  $30 \mu\text{m}$  in the lighter zones and  $35 \mu\text{m}$  in the darker zones. The dimension of the finite elements was  $0.1 \text{ mm}$ . Such a dimension is close to  $1/20$ th of the wavelength  $\lambda = 2 \text{ mm}$  at the analysed frequency.

In order to demonstrate efficiency of the proposed reconstruction methods of spatially non-uniform elastic properties three different cases with a hypothetical simple geometry were simulated—the mica paper sample with two zones of rectangular shape with different thickness and elastic properties (Figure 3), the sample with a single circular non-uniformity, and the sample with multiple circular non-uniformities of different diameters.

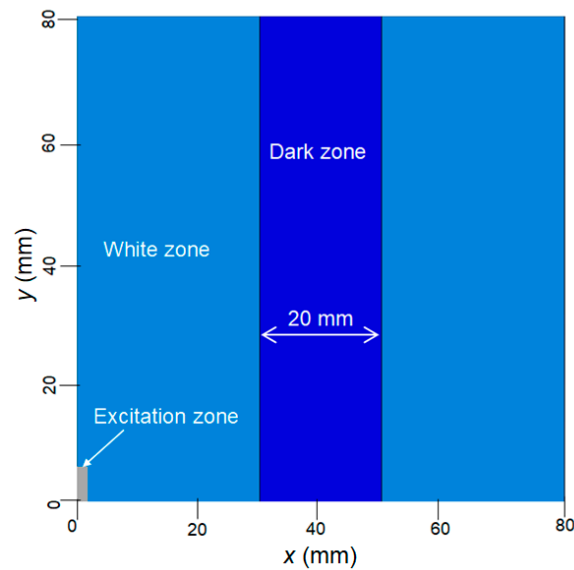


Figure 3. Sample of the mica paper with two zones with different elastic properties.

The simulated spatial distributions of the off-plane  $l$  particle velocity of the mica paper with the non-uniformity shown in Figure 3 at two different time instants  $t = 150 \mu\text{s}$  and  $246 \mu\text{s}$  after excitation are shown in Figure 4.

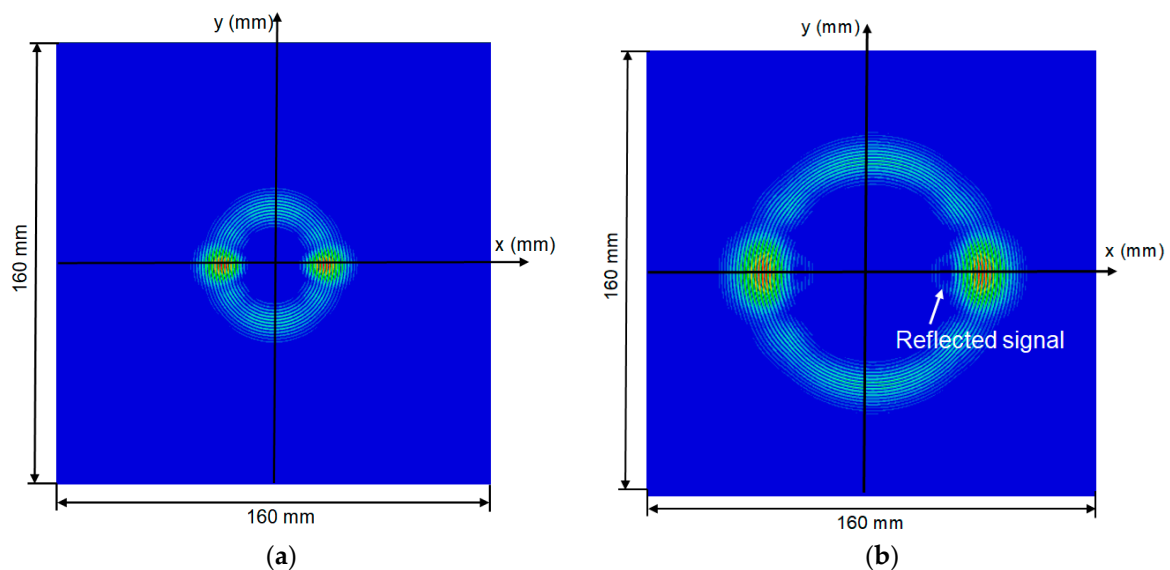
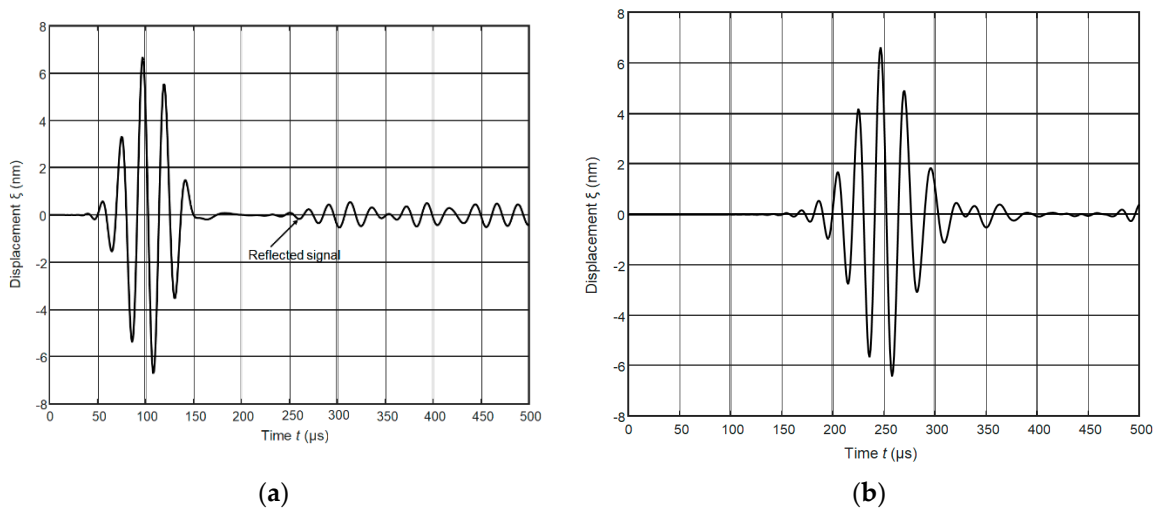


Figure 4. Spatial distributions of the normal particle velocity at two different time instants: (a)  $150 \mu\text{s}$ ; (b)  $246 \mu\text{s}$ .

As can be seen the waves are more strongly radiated along  $x$  axis direction due to directivity properties of the excitation zone. The weak pattern of the wave reflected by the boundary between zones with different properties can be observed at the time instant  $246 \mu\text{s}$  also. The waveforms of normal displacements at two different distances from the excitation area are shown in Figure 5 in which the tail of the main pulse of the signal is reflected by the border between the zones with different properties can be seen (Figure 5a).



**Figure 5.** Ultrasonic pulses at two different distances from the  $1 \times 5 \text{ mm}^2$  excitation zone: (a) 10 mm; (b) 40 mm.

### 3. The Zero-Crossing Reconstruction Method

A spatial distribution of elastic properties of the modelled MICA paper sample can be found from the reconstructed spatial distribution of the phase velocity of the  $A_0$  mode. For that the B-scan collected along the line  $y = 0$  (Figure 6) can be exploited.

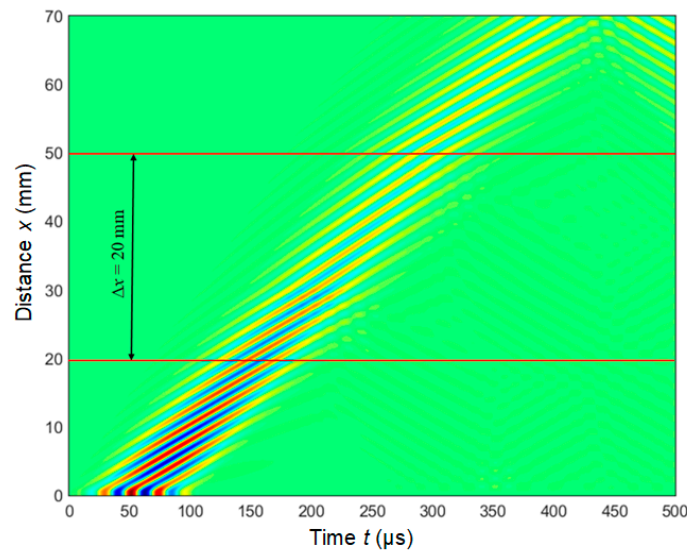


**Figure 6.** Simulated B-scan of the mica MICA paper with hypothetic two rectangular zones with different elastic properties and thickness. The horizontal dashed red lines indicate borders of the rectangular darker zone.

Thus, at first the variations of the phase velocity of ultrasonic waves along the propagation path should be determined. The phase velocity usually is found from the distance  $\Delta x_{ph}$  which was covered by a particular phase point during the time interval  $\Delta t_{ph}$ :

$$c_{ph} = \Delta x_{ph} / \Delta t_{ph} \tag{1}$$

In general, the B-scan is the set of the signals measured at different distances (Figure 6), then the phase velocity can be estimated by taking two signals measured at neighbouring positions and estimating the propagation time of a particular phase point between those positions. As in the B-scan

we have the signals measured at many positions along some direction, the variations of the phase velocity versus this direction can be determined also. The most reliable and most accurate phase points from the point of view of measurements are the zero crossing instants in the waveform of the signal. Reconstruction of the phase velocity variations along the selected propagation path is performed according to the following steps:

1. The multiple zero-crossing points in each signals are estimated using the method described in [28]. In such a way the set of zero crossing instants  $\{t_{k,n}\}$ , where  $k = 1 \div K$ ,  $K$  is the number of positions at which the signals were recorded;  $n = 1 \div N_k$ ,  $N_k$  is the number of instants at which the  $k$ -th signal crosses zero level;
2. The phase of the of guided waves signal is “moving” with respect to the envelop of the signals due difference of the phase and the group velocities. This is possible to see in the B-scan image. It may lead to the half-period errors in the selection of particular zero crossing point in two signals measured at neighbour positions. In order to avoid it, the estimated zero crossing time instants are sorted by following each particular zero crossing instant in the signals measured at different distances. The result is a new set  $\{t_{m,l}; x_{m,l}\}$ , where  $t_{m,l}$  are the new zero crossing time instants from the set  $\{t_{k,n}\}$ ;  $x_{m,l}$  is the distance at which the signals with particular the zero crossing time instant  $t_{m,l}$  was measured;  $m = 1 \div M$ ,  $M$  is the total number of the zero-crossing points followed up;  $l = 1 \div L_m$ ,  $L_m$  is the number of positions of particular time instants  $t_{m,l}$  followed up. The set  $\{t_{m,l}; x_{m,l}\}$  obtained in the case of the mica paper sample with a rectangular area with different properties in the graphical form is presented in Figure 9. The lines of a different colours indicate the different zero-crossing points followed-up.
3. The phase velocity versus distance is estimated according to  $c_{ph,m,l} = \frac{x_{m,l} - x_{m,l-1}}{t_{m,l} - t_{m,l-1}}$ . The obtained dependency separately for each followed up zero-crossing point is presented in Figure 7. The colours of the curves in Figure 7 correspond to the colours of the zero crossing points in Figure 9.
4. A smooth curve of the mean values of the phase velocity variations along the B-scan is calculated according to  $\bar{c}_{ph,m,l} = \text{mean}_l(c_{ph,m,l})$ . The reconstructed spatial distribution of the  $A_0$  mode phase velocity versus the distance  $x$  is presented in Figure 8.

The red vertical lines in Figures 7 and 8 indicate borders of the rectangular area in the mica sample with different properties.

From the reconstructed phase velocities the Young’s modulus can be found:

$$E = \frac{c^4 * 12\rho(1 - \nu^2)}{(2\pi fd)^2}. \quad (2)$$

In the analysed case in the rectangular darker zone the Young’s moduli  $E_D = 16$  GPa and the lighter zone  $E_L = 13$  GPa are obtained, which correspond to the input parameters of the finite element modelling. The obtained results indicate that in the case of non-uniformity with a simple geometry, for example of a rectangular shape, using the proposed method is possible to reconstruct a spatial distribution of the phase velocity and the Young’s modulus with a high accuracy.

We then check the efficiency of this approach in the case of non-uniformities of other shapes. The first case is a circular non-uniformity shown in Figure 10a by a darker colour.

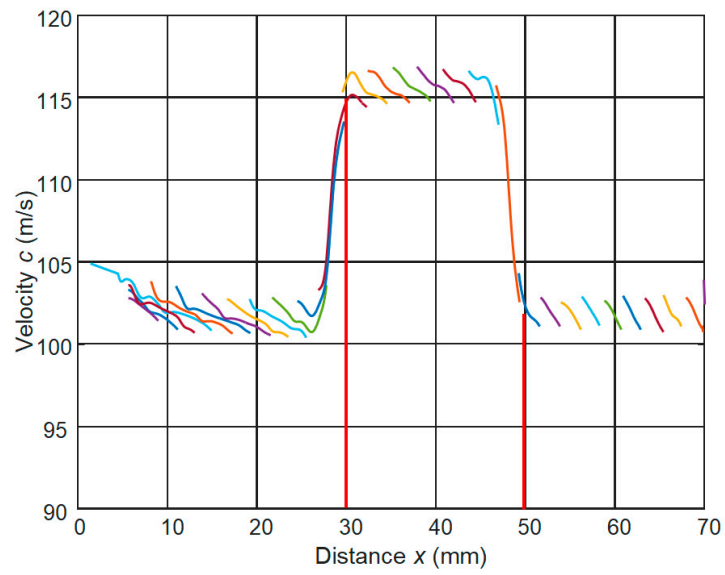


**Figure 7.** Spatial distributions of the  $A_0$  mode velocity along B-scan across the rectangular darker zone of the simulated mica sample. The different colours correspond to the results obtained from different zero-cross lines in Figure 9.

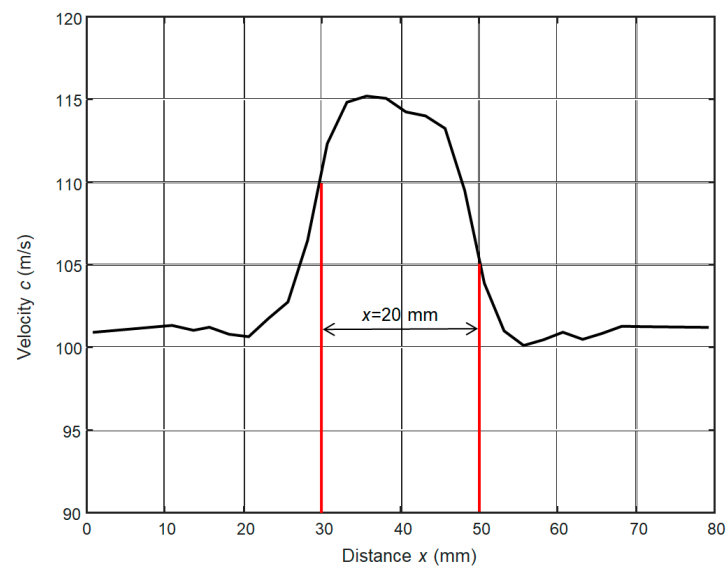


**Figure 8.** Mean value of the  $A_0$  mode velocity versus distance  $x$ .

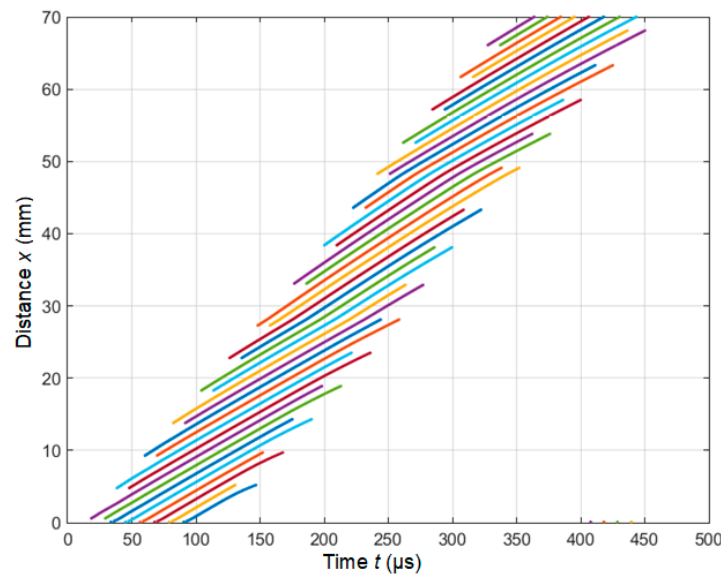


**Figure 9.** The zero-crossing instants of the normal displacements waveforms along the B-scan line.

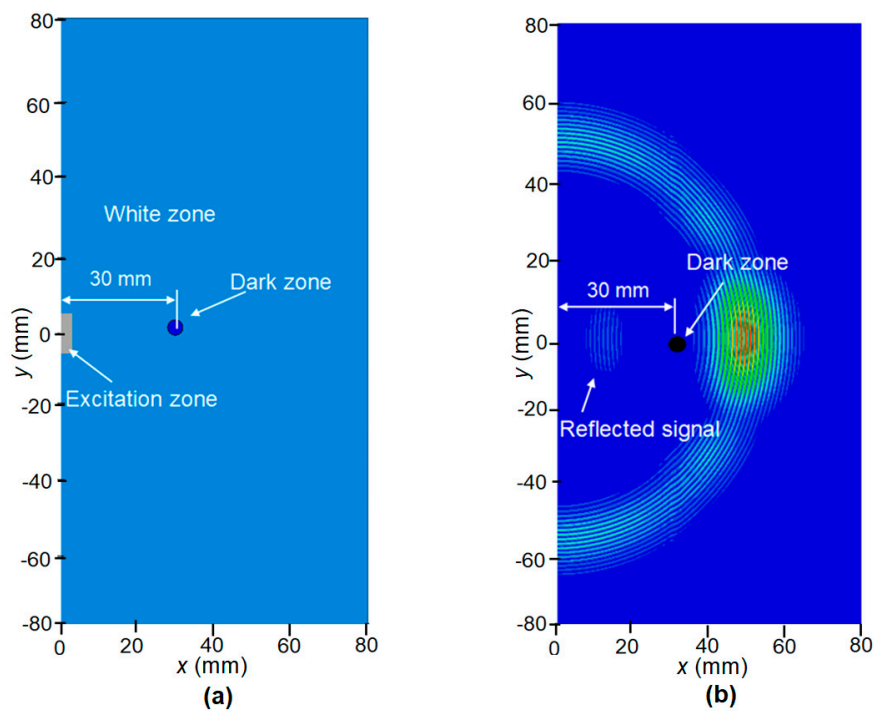


**Figure 10.** The sample of the mica paper with circular non-uniformity (a) and the snapshot of the spatial distribution of the ultrasonic pulsed field at the time instant  $t = 225 \mu s$  (b).

The diameter of this non-uniformity is 2 mm, e.g., comparable with the wavelength  $\lambda = (2 - 2.5)$  mm of the  $A_0$  mode in the mica paper sample. The elastic parameters and thickness are the same as in the case of the previous rectangular non-uniformity. The simulated spatial distribution of the of-plane displacements of the mica paper at the instant  $t = 225 \mu s$  is shown in Figure 10b. In the presented spatial distribution it is possible to see the ultrasonic signal reflected by the circular non-uniformity and propagating in a backward direction. The B-scan obtained along the line  $y = 0$  mm crossing the centre of the circular non-uniformity is presented in Figure 11a.

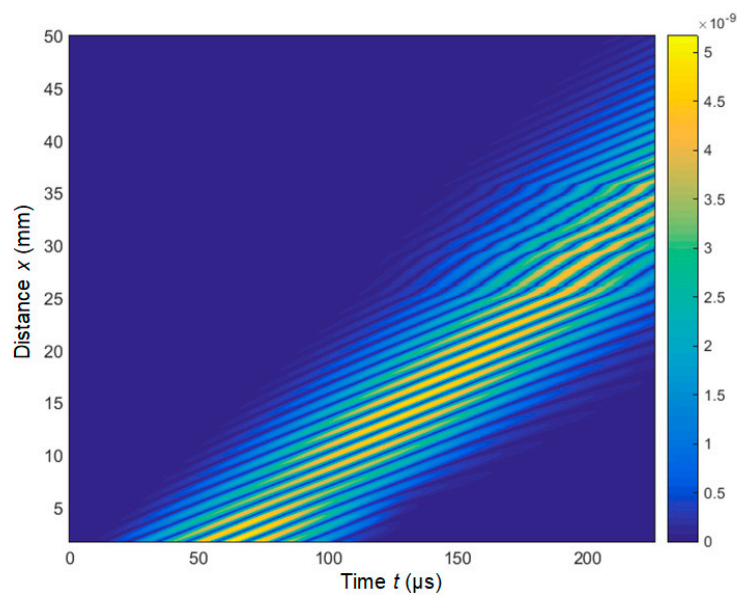
The reconstructed spatial distribution of the phase velocity obtained from the B-scan by the described zero-cross method is shown in Figure 11b. From the presented distribution follows that

velocities of the  $A_0$  mode are different in the circular non-uniformity and in the rest of the mica sample. Inside the non-uniformity the velocity is 110–115 m/s and outside 95–97 m/s. The spatial position of the ultrasound velocity peak exactly corresponds to the position of the circular non-uniformity. The presented example clearly shows ability of the described zero-crossing method to reconstruct correctly spatial distributions of  $A_0$  mode phase velocity even in the case of small size, e.g., comparable with the wavelength, non-uniformities.

We then analyse the case with a large number of circular non-uniformities of different diameters (Figure 12). This case is closest to the spatial distribution of zones with other properties of a real experimental mica specimen shown in Figure 13. The diameters of circular non-uniformities in simulation were selected randomly in the range 2–5 mm.

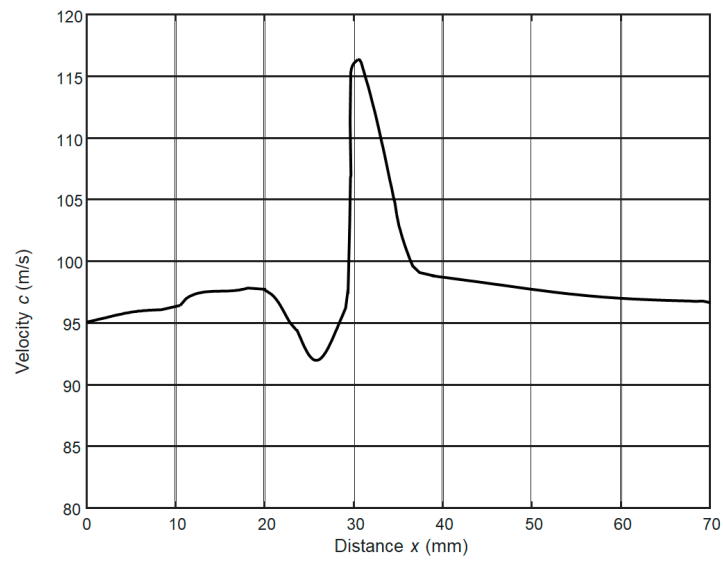
The simulated B-scan of normal displacements along  $x$  axis at  $y = 0$  is presented in Figure 14. The zero-crossing instants of the normal displacements waveforms along the B-scan line obtained by the described algorithm are shown in Figure 15.

The spatial distributions of the  $A_0$  mode phase velocity along the simulated B-scan at  $y = 0$  reconstructed by the presented algorithm in two zones 13–23 mm and 50–70 mm are shown in Figure 16a,b. These zones correspond to several circular non-uniformities which can be observed in Figure 12. The positions of those non-uniformities in Figure 16 are denoted by the red vertical lines. Variations of the phase velocity in those regions reach 95–117 m/s. The largest values of the phase velocity correspond to the darker non-uniformities with higher values of the Young's modulus.



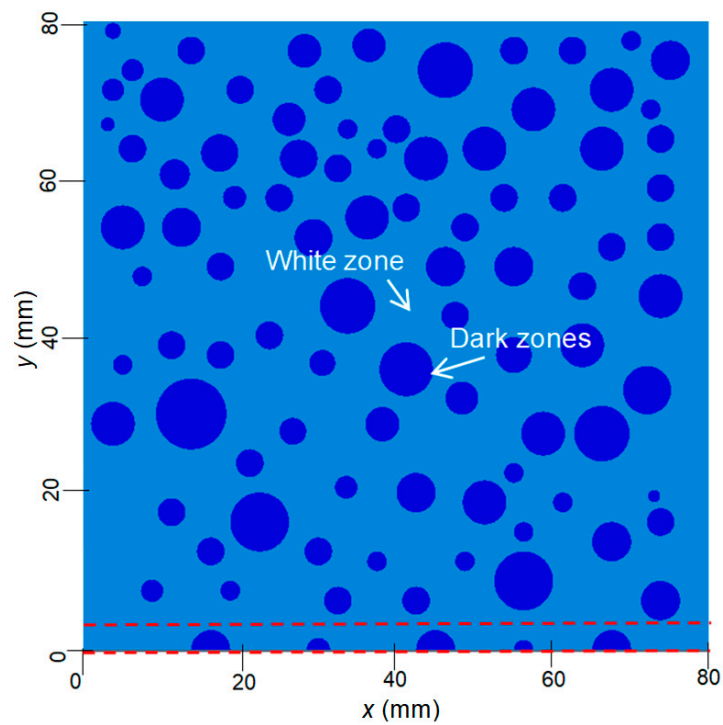
(a)

Figure 11. Cont.



(b)

**Figure 11.** Simulated B-scan of the MICA sample with a single circular non-uniformity (a) and spatial distribution of the phase velocity of  $A_0$  mode along the line  $y = 0$  mm in the case of the single circular non-uniformity (b).



**Figure 12.** 2D spatial distribution of circular non-uniformities in mica paper with dimensions  $80 \times 80$  mm (red lines are  $y = 0$  mm and  $y = 3$  mm).

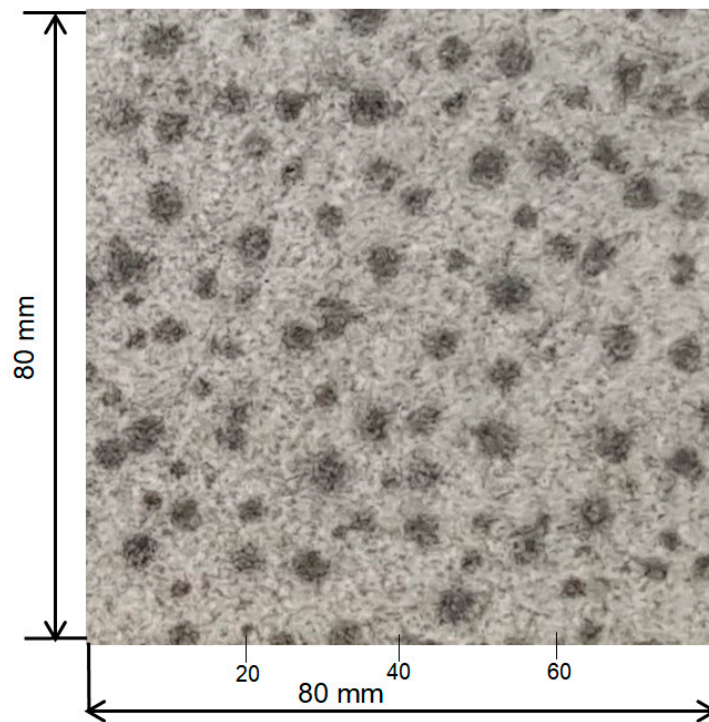


Figure 13. Mica paper sample with non-uniform elastic properties and thickness.

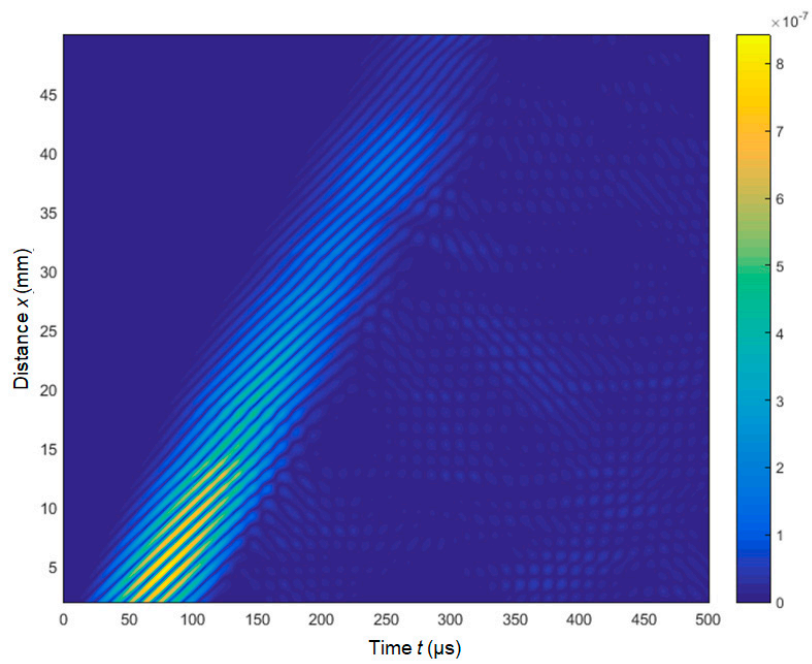
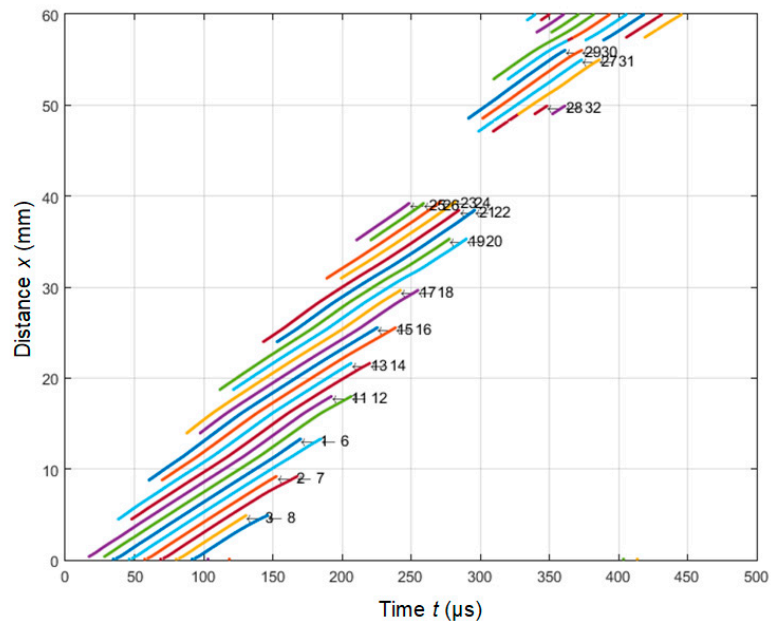
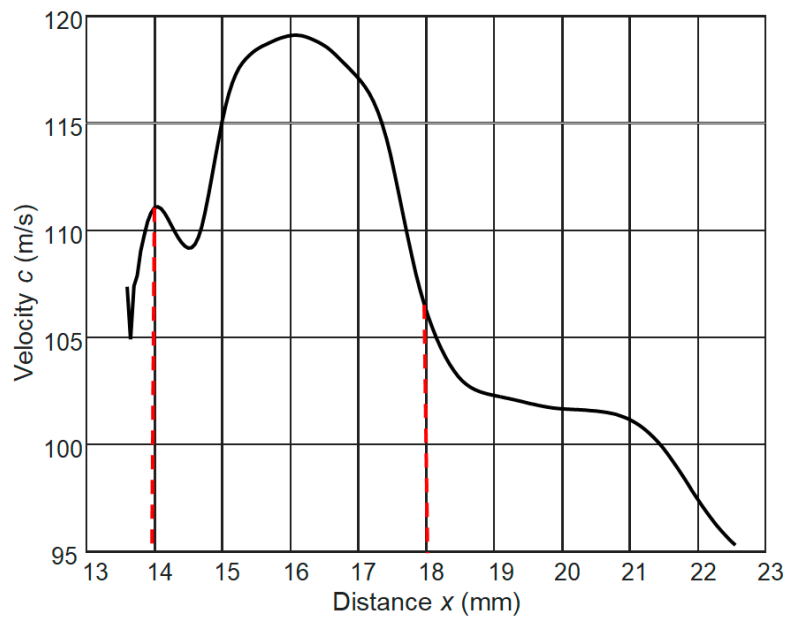


Figure 14. The simulated B-scan of the mica paper sample with multiple circular non-uniformities.

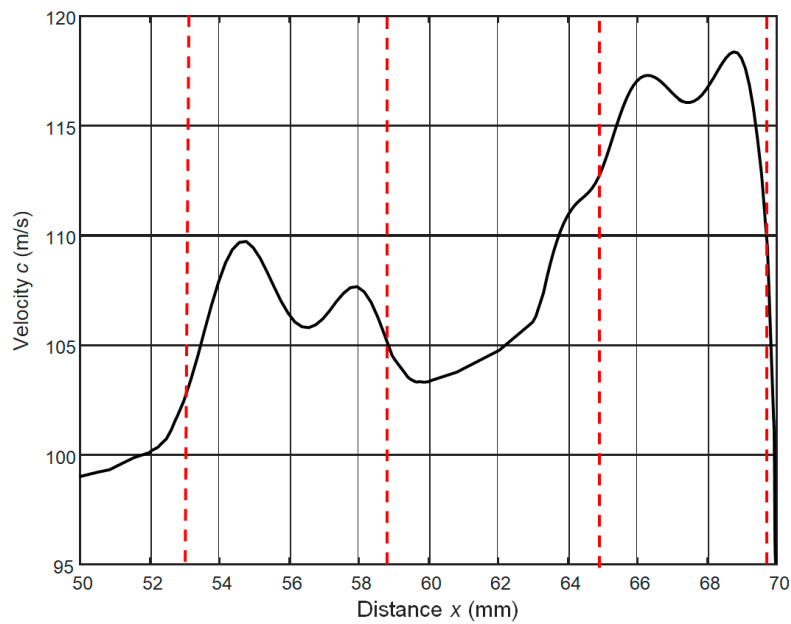


**Figure 15.** The zero-crossing instants of the normal displacements waveforms along the B-scan line in the mica paper sample with multiple circular non-uniformities.

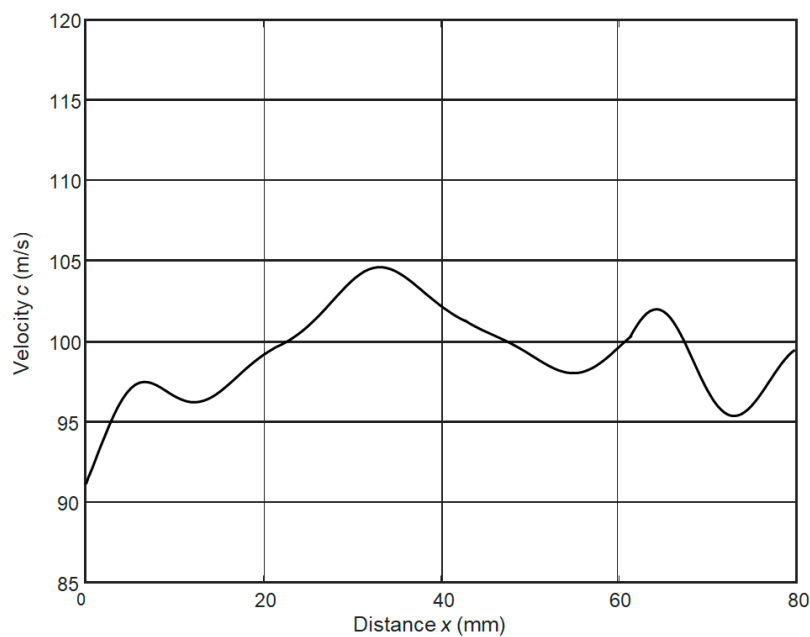


(a)

**Figure 16.** Cont.



(b)



(c)

**Figure 16.** The reconstructed spatial distributions of the  $A_0$  mode phase velocities along  $x$  axis in the case of the multiple circular non-uniformities: Figure 12,  $x = 13\text{--}23$  mm at  $y = 0$  mm—(a); Figure 12,  $x = 50\text{--}70$  mm at  $y = 0$  mm—(b); Figure 12,  $x = 0\text{--}80$  mm at  $y = 3$  mm—(c).

In Figure 16c the reconstructed phase velocity spatial distribution along the line  $y = 3$  mm which crosses the region with a smaller number of spatial non-uniformities is given. It is possible to see that in this region variations of the phase velocity are smaller in the range 95–104 m/s.

The presented results indicate that even in the case of multiple non-uniformities the zero-crossing method enables to obtain the phase velocity values both inside and the outside of the areas with non-uniform properties and to determine the spatial position of those non-uniformities.

#### 4. 2D Spatial–Temporal Spectrum Method

For identification of one or a few non-uniform areas in the sample under investigation we propose a method based on the analysis of a 2D spatial-temporal spectrum of the B-scan of normal displacements [26]. This spectrum is obtained by the 2D Fourier transform  $FFT_{2D}$  of the B-Scan data  $\xi(t, x)$ :

$$U(f, \lambda^{-1}) = FFT_{2D}[\xi(t, x)], \tag{3}$$

where  $f$  is the frequency and  $\lambda$  is the wavelength. The 2D spatial-temporal spectrum calculated using the B-scan measured along the line crossing the single circular non-uniformity (Figure 11) is presented in Figure 17. The colour scale of the amplitudes is shown on the right side of the image. In this figure two zones indicated by two rectangles show two waves  $A'_0$  and  $A''_0$  propagating with different velocities. Their amplitudes are shown by the colour scale on the right of Figure 17. The largest amplitudes are at a frequency of 45 kHz and spread along spatial frequencies  $\lambda^{-1}$ . The mode  $A'_0$  is concentrated around the spatial frequency  $\lambda^{-1} = 0.47 \text{ mm}^{-1}$  that corresponds approximately to the phase velocity 95 m/s. The  $A''_0$  mode is spread around the lower spatial frequency  $\lambda^{-1} = 0.37 \text{ mm}^{-1}$  and the corresponding phase velocity approximately is 120 m/s. From the presented results it is possible to see that the amplitude of the  $A'_0$  mode is higher than of the  $A''_0$  mode.

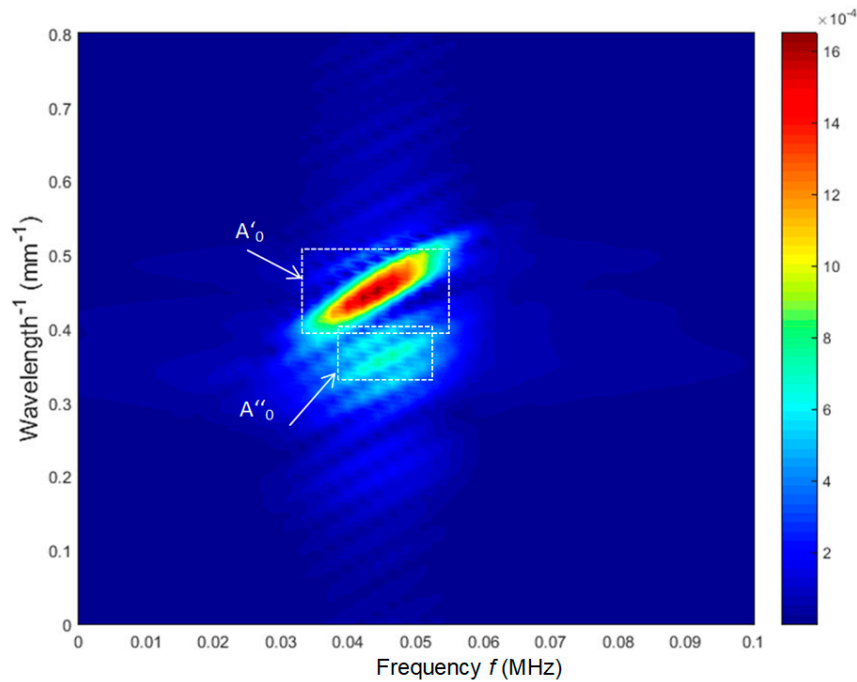


**Figure 17.** 2D spatial-temporal spectrum of the B-scan modes in the case of a single circular non-uniformity.

The presented results show that the discussed method enables revealing the presence of a few modes instead of one mode which usually propagates in uniform thin samples. The phase velocity  $c_{ph}$  of the  $A_0$  mode can be found from the well-known relation  $c_{ph}(f) = \lambda(f)f$ , where the wavelength  $\lambda$  is found from the 2D spatial temporal spectrum at the selected frequency  $f$ . Thus, this method is based on the exploitation of different propagation velocities of those waves.

The waves with different phase velocities can be separated by a 2D spatial-temporal band-pass filter:

$$U_f(f, \lambda^{-1}) = U(f, \lambda^{-1}) \cdot H_f(f, \lambda^{-1}), \tag{4}$$

where  $H_f(f, \lambda^{-1})$  is the spatial-temporal response of the filter. The cut-off spatial and temporal frequencies of the filter are chosen according to the mode which should be separated. The cut-off spatial

frequencies  $\lambda^{-1}$  are  $0.35 \text{ mm}^{-1}$  and  $0.53 \text{ mm}^{-1}$  shown in Figure 17. Correspondingly, the temporal cut-of frequencies are 30 kHz and 60 kHz.

The filtered B-Scan  $\xi_f(t, x)$  is obtained by the inverse 2D Fourier transform:

$$\xi_f(t, x) = FFT_{2D}^{-1}[U_f(f, \lambda^{-1})]. \tag{5}$$

From the analysis presented follows that the modes with different phase velocities can be separated applying 2D filtering of the 2D spectrum. However, if the spatial or temporal narrow band filtering is used then according to the uncertainty principle the spatial resolution  $\Delta x$  is lost:

$$\lambda_x^{-1} \cdot x \approx 1, \tag{6}$$

where  $\Delta\lambda_x^{-1}$  is the bandwidth of the 2D filter in the spatial domain. It means that in this case it is impossible to get spatial dependence of the phase velocity versus distance  $x$  and only the average ultrasound velocity  $\bar{c}$  along the selected distance  $\Delta x = x_2 - x_1$  can be obtained:

$$\bar{c} = \frac{1}{\Delta x} \int_{x_1}^{x_2} c(x) dx. \tag{7}$$

Let us analyse the case with a big number of circular non- uniformities of different diameters (Figure 12). The simulated B-scan of normal displacements along  $x$  axis ( $y = 0$ ) is shown in Figure 14. The corresponding 2D spectrum of the B-scan is presented in Figure 18.

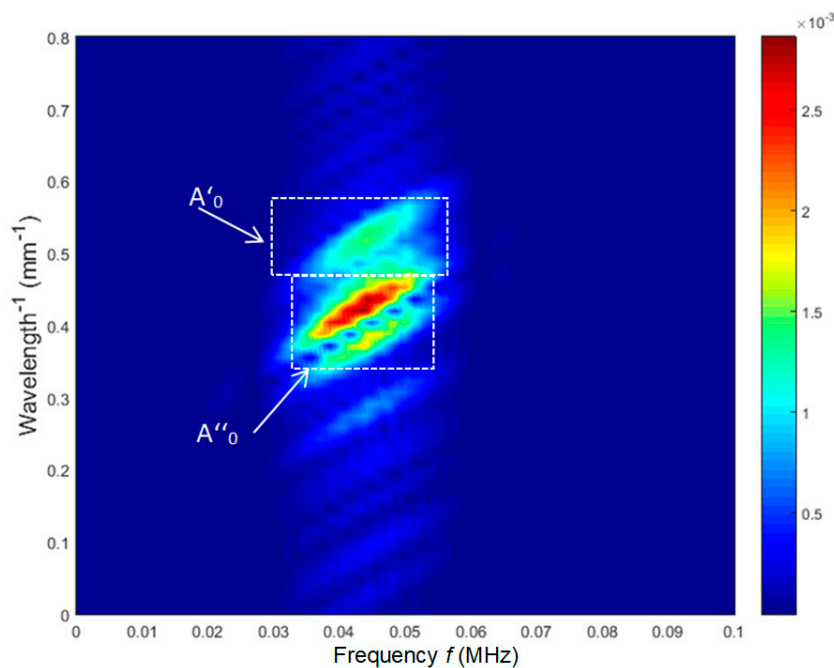


**Figure 18.** 2D spatial-temporal spectrum of the B-scan mode in the case of a multiple circular non-uniformities ( $t = 20:400 \mu s$ ,  $y = 3 \text{ mm}$ ).

From the presented spectrum it follows that it is possible to identify a few  $A_0$  modes propagating with different velocities in the case of multiple circular non-uniformities as well.

### 5. Experimental Results

The results of the theoretical analysis were verified by experimental investigations. They were carried out with the experimental mica specimen with clearly expressed non-uniform properties (Figure 13). In this sample the sub-sonic  $A_0$  mode was excited and the spatial distributions of

the of-plane displacements of the mica paper were measured by the laser interferometer using the experimental setup presented in Figure 19. The experimental setup was the same as used for investigation of PVC samples [29].

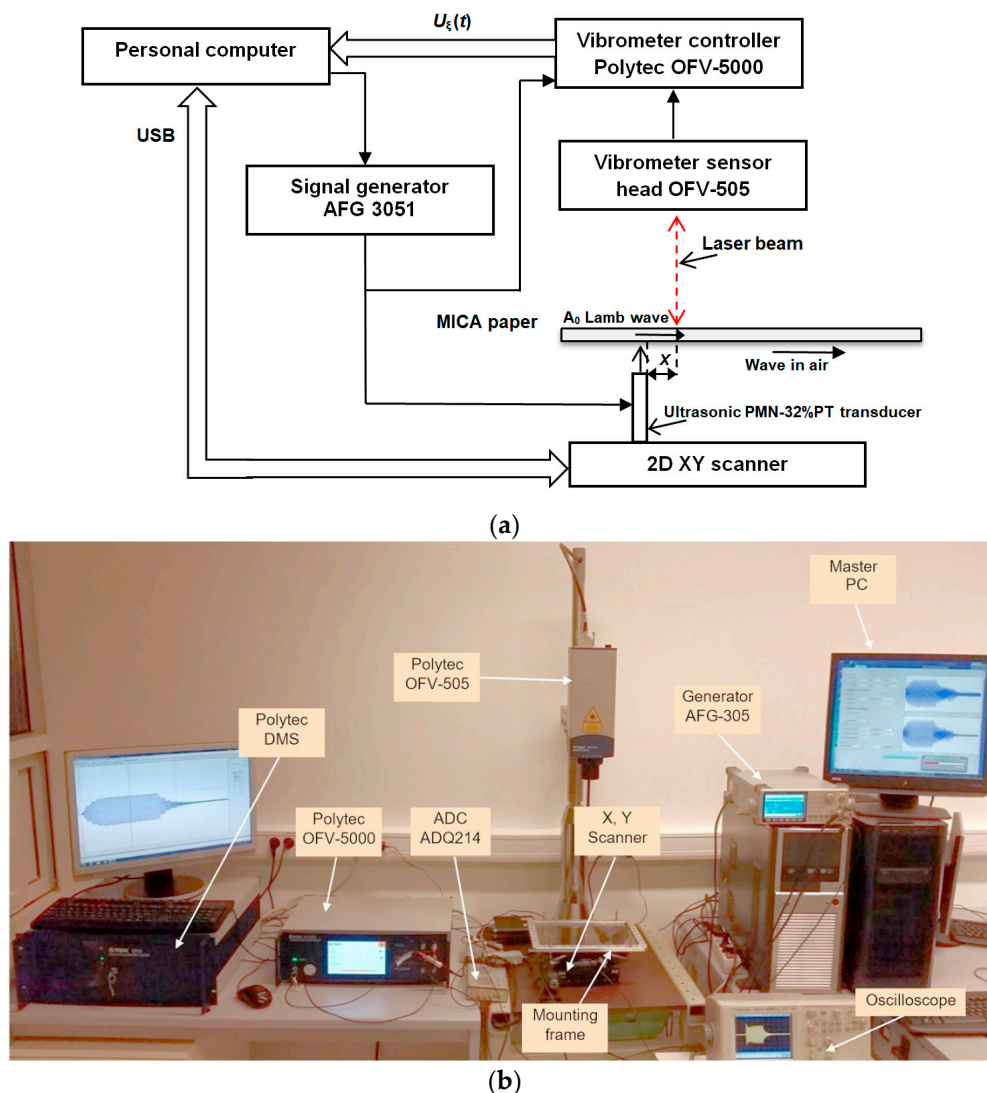
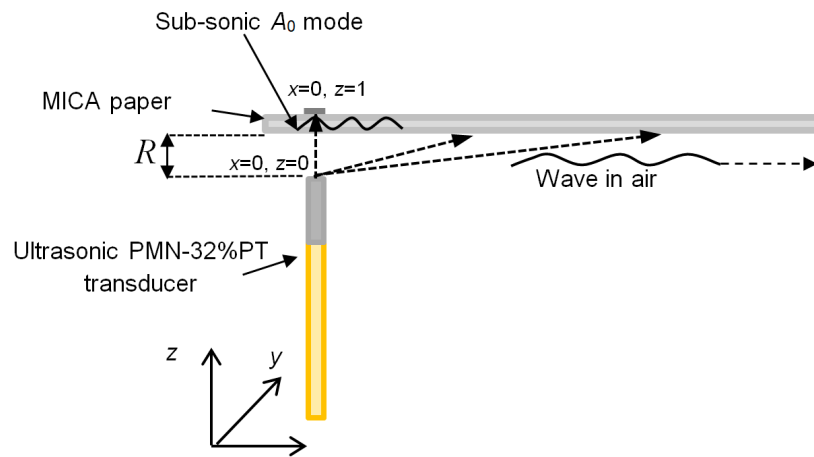


Figure 19. Experimental setup.

For determination of elastic properties of the mica paper a slow sub-sonic  $A_0$  mode guided wave is excited by a contact or by an air-coupled PMN-32%PT ultrasonic transducer (Figure 19). For measurements a pulse-type excitation is used. The off-plane displacements  $\xi$  of the plate surface caused by the propagating wave are picked up along the selected lines, for example, parallel to the coordinate  $x$ , and in this way the B-scan is formed  $\xi(x_j, t)$ , where  $j = 1 \dots N$  are the numbers of measurement points. The step between the measurement points is chosen according to the expected dimensions of the spatial non-uniformities, e.g., it should be shorter at least by one order. The obtained primary B-scan is processed by the two proposed signal processing methods described above.

Ultrasonic guided waves in the mica sample were excited by the PMN32%PT strip-like transducer with the aperture  $5 \times 1$  mm operating in the frequency range 43–48 kHz. The same transducer was used as a dry contact and air-coupled transducer. In the first case the transducer was contacting the mica sample, and in the second case between there was an air gap between the transducer and mica sample of  $R = 0.5$  mm (Figure 20).



**Figure 20.** Excitation of the  $A_0$  mode via air gap.

In the last case the excitation area is lightly spread in space, but due to the narrow air gap between the tip of the ultrasonic transducer and the sample the amplitude of the lateral air wave is rapidly reducing. During experiments B-scans were registered by a POLYTEC laser interferometer in different zones of the mica sample. The propagation of guided  $A_0$  mode signals is accompanied by the attenuation and scattering of ultrasonic waves.

Experiments were performed on the mica A4 dimensions sample with the thickness  $35\ \mu\text{m}$ . The sample together with the contact PMN-32%PT strip-like transducer was scanned with respect to the laser beam with a step of  $0.1\ \text{mm}$ . Interferometer averaging was set three times. The B-scans were collected in different areas of the sample in order to randomize the influence of the optically darker zones which possess very different acoustic properties. The length of the B-scans was  $85\ \text{mm}$ . The duration of ultrasonic pulse used for excitation of  $A_0$  mode was six periods, and the central frequency was  $44\ \text{kHz}$ . The example of the recorded raw B-scan in the case of the contact excitation is presented in Figure 21.

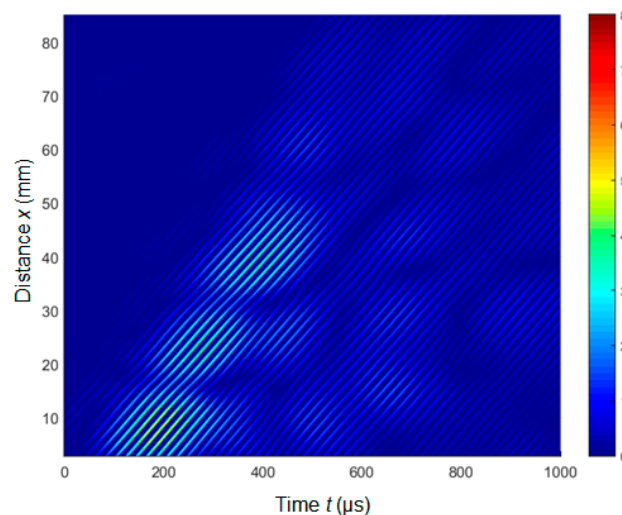


**Figure 21.** The B-scan obtained in the case of the contact excitation ( $y = 0\ \text{mm}$ ).

The 2D spectra of the B-scans obtained in the case of the contact and the air-coupled excitation are presented in Figure 22a,b.

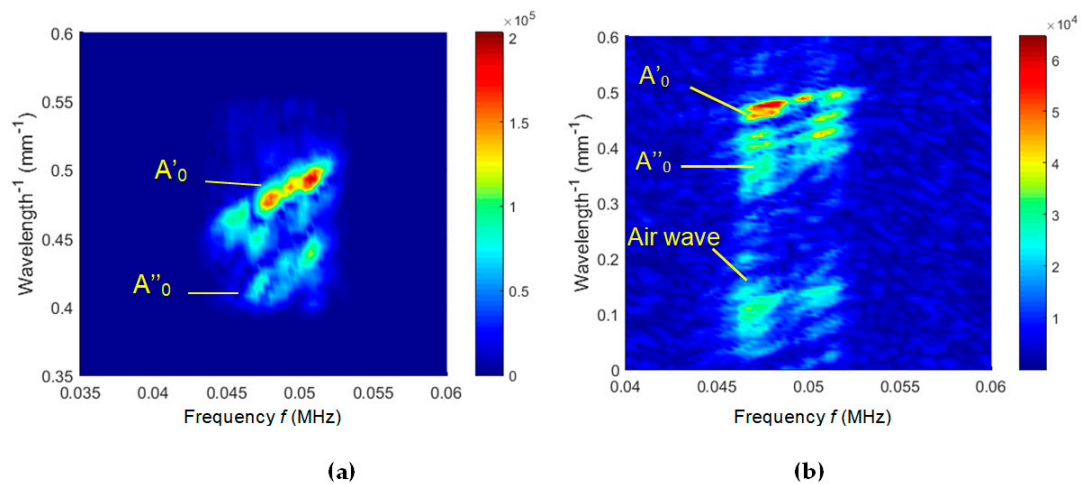


**Figure 22.** 2D spectra of the contact (a) and of the air-coupled B-scans (b).

In both cases presence of a few modes with different phase velocities is seen. The largest amplitudes are at a frequency of 46 kHz and distributed along spatial frequencies  $\lambda^{-1}$  in the range of [0.45–0.5] mm<sup>-1</sup>.

In the case of a contact excitation the *A*'<sub>0</sub> and *A*''<sub>0</sub> modes are due to the zones with different elastic properties and thickness. The obtained experimental results are very close to the results of the numerical modelling (Figure 18).

In the case of the air-coupled excitation in addition to those modes the wave propagating in air originates from the tip of the air-coupled transducer. In the 2D spatial–temporal spectrum the spatial frequencies in the range [0.05–0.1] mm<sup>-1</sup> correspond to the wave propagating in air. The propagation paths of this wave are shown in Figure 20.

The spatial distribution of the *A*<sub>0</sub> mode phase velocity obtained from the experimentally collected B-scan in the case of the contact excitation is presented in Figure 23. The B-scan was measured along the *x* axis from the centre of the excitation aperture of the piezoelectric transducer. The spatial reconstruction of the phase velocity was performed by the proposed zero-crossing method. From the presented distribution follows that variations of the phase velocity are in the range 91–109 m/s and the highest values correspond to the positions of the optically darker spots (Figure 13) with higher values of the Young's modulus of  $E_D = 13$  GPa. Correspondingly, in the lighter zones the Young's modulus is  $E_L = 9$  GPa. The Young's moduli values were found using Equation (2).

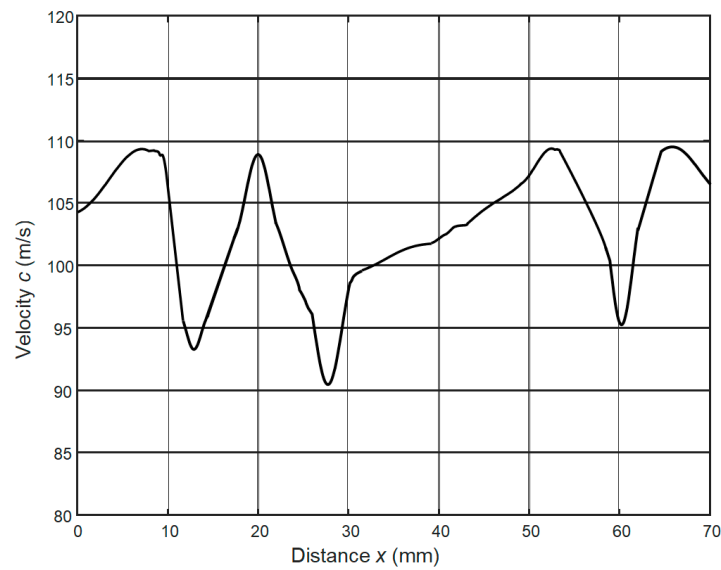


Figure 23. Spatial distribution of the phase velocity reconstructed from the contact B-scan.

For more detailed analysis the  $A'_0$  and  $A''_0$  modes obtained in the case of the air-coupled excitation were selected (Figure 24).

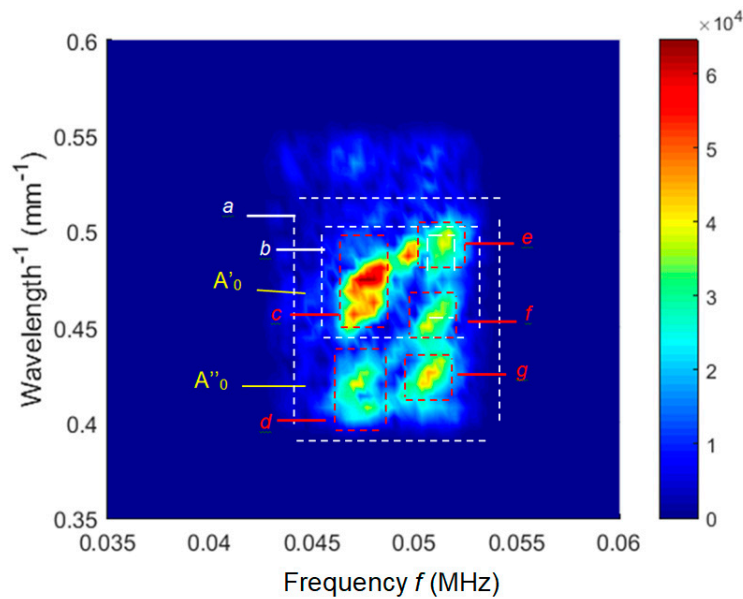


Figure 24. 2D spectrum of the air-coupled B-scan of the sample.

The phase velocities of different  $A_0$  modes propagating in the sample obtained from the 2D spectrum presented in Figure 24 are presented in Table 1. The modes  $A''_0$  propagate with a higher velocity and are caused by the darker zones in the mica specimen.

**Table 1.** Phase velocities of different modes.

Zone in Figure 24	Mode Name	Spatial Frequency Range, $\text{mm}^{-1}$	Frequency Range, kHz	Phase Velocities $c$ , m/s
a	$A'_0, A''_0$	0.4–0.55	43.11–53.31	100–112
b	$A'_0$	0.45–0.51	46.02–52.35	95–103
c	$A'_0$	0.45–0.48	46.02–49.02	96–102
d	$A''_0$	0.40–0.43	46.02–48.35	111–112
e	$A'_0$	0.48–0.51	51.02–52.35	104
f	$A'_0$	0.44–0.47	50.02–52.02	111–112
g	$A''_0$	0.41–0.44	49.35–51.68	118–121

It is necessary to point out that the B-scans recorded in different zones of the MICA sample are slightly different due different number and dimensions of the optically darker zones (Figure 13) the physical properties of which differ from the optically lighter zone.

## 6. Conclusions

For evaluation of spatial distributions of non-uniform elastic properties of thin plates and films the method based on measurement of local phase velocities of a sub-sonic  $A_0$  mode Lamb wave was proposed. The phase velocities are found from the B-scans by two proposed signal processing methods—the zero crossing method and analysis of the 2D spatial–temporal spectrum of the B-scan. The sub-sonic  $A_0$  mode is excited by the contact or air-coupled ultrasonic transducer made of a PMN-32%PT piezoelectric element with a small  $5 \times 1$  mm aperture. The off-plane displacements caused by the  $A_0$  mode are measured by a POLYTEC laser interferometer at different distances from the excitation area and in this way the B-scan is obtained. The combination of air-coupled excitation and contactless reception, in principle, allows measurements of moving objects and hygroscopic materials.

The efficiency of the proposed signal processing methods was evaluated theoretically and experimentally using thin mineral mica paper sheets with non-uniform in-plane properties. The theoretical evaluation was carried out using simulation results obtained by a finite element modelling for three hypothetical cases—the mica paper sample with two zones of rectangular shape with different thickness and elastic properties, the sample with a single circular non-uniformity, and the sample with multiple circular non-uniformities of different diameters. The processing of the simulated B-scans by the both proposed methods showed that they allow obtaining the spatial distribution of the local phase velocity, from which such elastic properties such as the Young's module can be evaluated. Experiments performed with the mica paper samples confirmed results of the theoretical investigations.

The performed investigations also showed that, in the case of the non-uniformities with properties different from the rest of the sample under investigation instead of one basic  $A_0$  mode, a few  $A_0$  modes with different phase velocities originate. That can be rapidly found by the analysis of the 2D spatial-temporal spectrum. The velocities of those waves can be determined by both signal processing methods. The difference between them is that the zero-crossing method allows getting spatial distributions of the local phase velocities at one operation frequency and the 2D spectrum method enables the determination of the phase velocity at any temporal frequency; however, the spatial resolution in this case is lost. In the investigated mica sample two  $A_0$  modes with different phase velocities were found. One mode propagates with the phase velocities  $c_{ph1} = (95 \pm \Delta 3)$  m/s and another one with the phase velocities  $c_{ph2} = (106 \pm \Delta 6)$  m/s at a frequency of 47 kHz. The reconstructed Young's modulus values are in the range of 9–13 GPa. The variations of the phase velocities  $\pm \Delta c$  are due to the random character of non-uniformities in the mica sample and depend on the area in the sample in which the measurements are performed.

**Author Contributions:** Conceptualization: R.J.K. and L.M.; methodology: R.J.K.; validation: J.S.; formal analysis: J.S. and L.M.; investigation: J.S.; writing—original draft preparation: R.J.K.; writing—review and editing: J.S., L.M., and R.J.K.; project administration: R.J.K.; funding acquisition: R.J.K. All authors have read and agreed to the published version of the manuscript.

**Funding:** This research was funded by Lithuanian Research Council under project agreement no. P-MIP-17-37.

**Conflicts of Interest:** The authors declare no conflict of interest.

## References

1. Gómez Álvarez-Arenas, T.E.; Soto, D.A. Characterization of mineral paper by air-coupled ultrasonic spectroscopy. *Ultrasonics* **2012**, *52*, 794–801. [[CrossRef](#)] [[PubMed](#)]
2. Worlton, D.C. Ultrasonic testing with Lamb waves. *Non Destr. Test.* **1957**, *15*, 218–222.
3. Rose, J.L. *Ultrasonic Waves in Solid Media*; Cambridge University Press: Cambridge, UK, 1999; pp. 3–32.
4. Rose, J.L. Standing on the shoulders of giants: An example of guided wave inspection. *Mater. Eval.* **2002**, *60*, 53–59.
5. Böttger, W.; Schneider, H.; Weingarten, W. Prototype EMAT system for tube inspection with guided ultrasonic waves. *Nucl. Eng. Des.* **1987**, *102*, 369–376. [[CrossRef](#)]
6. Rose, J.L.; Soley, L. Ultrasonic guided waves for the detection of anomalies in aircraft components. *Mater. Eval.* **2000**, *50*, 1080–1086.
7. Neuenschwander, J.; Furrer, R.; Roemmeler, A. Application of air-coupled ultrasonics for the characterization of polymer and polymer-matrix composite samples. *Polym. Test.* **2016**, *56*, 379–386. [[CrossRef](#)]
8. Hirao, M.; Ogi, H. An SH-Wave EMAT Technique for Gas Pipeline Inspection. *Ndt E Int.* **1999**, *32*, 127–132. [[CrossRef](#)]
9. Quaegebeur, N.; Masson, P.; Berry, A.; Ardin, C.; D’Anglade, P.-M. Ultrasonic non-destructive testing of cardboard tubes using air-coupled transducers. *NDT E Int.* **2018**, *93*, 18–23. [[CrossRef](#)]
10. Fan, Z.; Jiang, W.; Cai, M.; Wright, W.M. The effects of air gap reflections during air-coupled leaky Lamb wave inspection of thin plates. *Ultrasonics* **2016**, *65*, 282–295. [[CrossRef](#)]
11. Sen, N.; Kundu, T. A new wave front shape-based approach for acoustic source localization in an anisotropic plate without knowing its material properties. *Ultrasonics* **2018**, *87*, 20–32. [[CrossRef](#)]
12. Kazys, R.J.; Vilpisauskas, A.; Šeštoke, J. Application of Air-Coupled Ultrasonic Arrays for Excitation of a Slow Antisymmetric Lamb Wave. *Sensors* **2018**, *18*, 2636. [[CrossRef](#)] [[PubMed](#)]
13. Hongchen, M.; Faxin, L. Excitation and reception of non-dispersive guided waves using face-shear  $d_{24}$  mode piezoelectric transducers. In Proceedings of the Nondestructive Characterization and Monitoring of Advanced Materials, Aerospace, and Civil Infrastructure, Portland, OR, USA, 26–29 March 2017; pp. 1–13.
14. Mazzotti, M.; Marzani, A.; Bartoli, I. Dispersion analysis of leaky guided waves in fluid-loaded waveguides of generic shape. *Ultrasonics* **2014**, *54*, 408–418. [[CrossRef](#)] [[PubMed](#)]
15. Chimenti, D.E.; Martin, R.W. Nondestructive evaluation of composite laminates by leaky Lamb waves. *Ultrasonics* **1991**, *29*, 13–20. [[CrossRef](#)]
16. Chimenti, D.E. Review of air-coupled ultrasonic materials characterization. *Ultrasonics* **2014**, *54*, 1804–1818. [[CrossRef](#)]
17. Panda, R.S.; Rajagopal, P.; Balasubramaniam, K. Characterization of delamination-type damages in composite laminates using guided wave visualization and air-coupled ultrasound. *Struct. Health Monit.* **2017**, *16*, 142–152. [[CrossRef](#)]
18. Raišutis, R.; Kažys, R.; Žukauskas, E.; Mažeika, L. Ultrasonic air-coupled testing of square-shape CFRP composite rods by means of guided waves. *NDT E Int.* **2011**, *44*, 645–654. [[CrossRef](#)]
19. Mei, H.; Haider, M.F.; Joseph, R.; Migot, A.; Giurgiutiu, V. Recent advances in piezoelectric wafer active sensors for structural health monitoring applications. *Sensors* **2019**, *19*, 383. [[CrossRef](#)]
20. Castaings, M.; Cawley, P.; Farlow, R.; Hayward, G. Single sided inspection of composite materials using air coupled ultrasound. *J. Nondestruct. Eval.* **1998**, *17*, 37–45. [[CrossRef](#)]
21. Kazys, R.; Stolpe, P. Ultrasonic non-destructive on-line estimation of the tensile strength of a running paper web. *NDT E Int.* **2001**, *34*, 259–267. [[CrossRef](#)]
22. Alers, G.A.; Burns, L.R. EMAT Designs for Special Applications. *Mater. Eval.* **1987**, *45*, 1184–1194.

23. Mohr, W.; Höller, P. On Inspection of Thin Walled Tubes for Transverse and Longitudinal Flaws by Guided Ultrasonic Waves. *IEEE Tran Sonics Ultrason.* **1976**, *23*, 369–373. [[CrossRef](#)]
24. Schindel, D.W.; Hutchins, D.A. Applications of micromachined capacitance transducers in air-coupled ultrasonics and nondestructive evaluation. *IEEE Trans. Ultrason. Ferroelectr. Freq. Control* **1995**, *42*, 51–58. [[CrossRef](#)]
25. Salzburger, H.-J.; Dobmann, G.; Mohrbacher, H. Quality Control of Laser Welds of Tailored Blanks Using Guided Waves and EMATs. *IEE Proc. Sci. Meas. Technol.* **2001**, *148*, 143–148. [[CrossRef](#)]
26. Kazys, R.J.; Mazeika, L.; Šliteris, R.; Sestoke, J. Air-Coupled Excitation of a Slow  $A_0$  Mode Wave in Thin Plastic Films by an Ultrasonic PMN-32%PT Array. *Sensors* **2018**, *18*, 3156. [[CrossRef](#)]
27. Kazys, R.J.; Vilpisauskas, A. Air-Coupled Reception of a Slow Ultrasonic  $A_0$  Mode Wave Propagating in Thin Plastic Film. *Sensors* **2020**, *20*, 516. [[CrossRef](#)]
28. Draudviliene, L.; Meskuotiene, A.; Mazeika, L.; Raišutis, R. Assessment of quantitative and qualitative characteristics of ultrasonic guided wave phase velocity measurement technique. *J. Nondestruct. Eval.* **2017**, *36*, 1–13. [[CrossRef](#)]
29. Kažys, R.; Šliteris, R.; Mažeika, L.; Tumšys, O.; Žukauskas, E. Attenuation of a Slow Subsonic  $A_0$  Mode. Ultrasonic Guided Wave in Thin Plastic Films. *Materials* **2019**, *12*, 1648. [[CrossRef](#)]



© 2020 by the authors. Licensee MDPI, Basel, Switzerland. This article is an open access article distributed under the terms and conditions of the Creative Commons Attribution (CC BY) license (<http://creativecommons.org/licenses/by/4.0/>).